this dip was not caused by a ring or small body near Neptune. The other three notable dips in signal that occur after 3:25 UTC were apparently not caused by continuous equatorial rings either, as this region was probed during the 10 May event, with negative results. In fact, the dip at 3:25 UTC occurred when the planet was near the edge of the photometer beam. Other than the dips just discussed and the occultation by Neptune, the signal never drops below 0.93 of its unocculted value. Hence, we place a limit of 0.07 on the optical depth of any equatorial rings of Neptune, with widths >5 km and radii $>31{,}400$ km.

Our upper limit is about four times lower than would have been necessary to detect the least opaque uranian ring (ring 6), but we could not have detected a jovian-type ring, of low optical depth. (The jovian ring has not yet been detected by radio or optical occultation[27,28].) Hence, in terms of detectability by occultations, any system of rings around Neptune must be much less extensive than the uranian system.

In terms of the amount of material that could exist as neptunian rings, our limit on the optical depth allows a large range of masses. On one hand, we could have detected as little as 10^{12} g of material concentrated into a narrow ring. However, the form of the material least amenable to detection by our observations would be a collection of small satellites, ~ 1 km in diameter. This diameter would be too small for an individual satellite to cause an observable occultation. If the mean optical depth of the collecton of satellites were <0.07, we would not have detected the ensemble either. If the material were carbonaceous ($\rho = 3$ g cm^{-3}), the combined mass of these satellites could be as great as 4×10^{23} g. This is comparable to recent upper limits on the mass of Saturn's rings[29] and would equal that of a single satellite, 600 km in diameter.

Conclusions

It is puzzling to reconcile our failure to detect rings with the recent discovery (through occultation observations) of an apparently small, third satellite of Neptune[30], with an orbital radius of 3 R_N. As the odds against discovering a lone body in this manner would be so great, one might conclude that Neptune has several, if not many, small satellites. One small satellite orbits just inside, and another just outside, the F ring of Saturn; at least two exist near Jupiter's ring and several small satellites have been postulated to be intimately associated with the uranian rings.

Hence we must still entertain the possibility of a neptunian ring system that we were unable to detect. A further opportunity to search for rings with occultations, with better sensitivity, occurs[17] in 1983, and Voyager encounters Neptune in 1989. If these opportunities fail to reveal rings, then we need wait only $\sim 10^8$ yr until tidal interaction between Neptune and Triton will have caused Triton to move close enough to Neptune to break up into what should be a spectacular system of rings[31].

We thank the telescope allocation committees of Mauna Kea, the IRTF, Mount Stromlo and Siding Spring for our observing time and B. Schaefer, F. Cheigh, G. Martin, R. Smith and D. Zarro for observational assistance. This work was partially supported by grants from NSF (AST-7827879 and AST-8010699) and NASA (NSG-7526 and NSG-7603).

Note added in proof: An error of $2\frac{1}{3}$ was found by P.D.N. in Smoluchowski's expression for the upper accretion limit[22]. For $\rho = 1$ gm cm^{-3}, the correct radius of the upper accretion limit in Fig. 1 is 66,500 km (not 83,800 km).

Received 31 August; accepted 25 September 1981.

1. Elliot, J. L. *A. Rev. Astr. Astrophys.* **17,** 445 (1979).
2. Goldreich, P. & Tremaine, S. *Nature* **277,** 97 (1979).
3. Dermott, S. F., Murray, C. D. & Sinclair, A. T. *Nature* **284,** 309 (1980).
4. Smith, B. A. *et al. Science* **206,** 927 (1979).
5. Smith, B. A. *et al. Science* **212,** 163 (1981).
6. Baum, R. *The Planets, Some Myths and Realities*, 120 (David and Charles, Newton Abbot, 1973).
7. Smoluchowski, R. *Commun. Astrophys.* **8,** 69 (1979).
8. Pollack, J. B. *Space Sci. Rev.* **18,** 3 (1975).
9. Ip, W.-H. *Space Sci. Rev.* **26,** 39 (1980).
10. Ip, W.-H. *Space Sci. Rev.* **26,** 97 (1980).
11. Dermott, S. F. *Phil. Trans R. Soc.* (in the press)
12. Prentice, A. J. R. & ter Haar, D. *Moon Planets* **21,** 43 (1979).
13. Morrison, D. Cruikshank, D. P. & Burns, J. A. in *Planetary Satellites* (ed. J. A. Burns) 3 (University of Arizona Press, 1977).
14. Elliot, J. L. in *Uranus and the Outer Planets* (ed. G. A. Hunt) (Cambridge University Press, in the press).
15. Dobrovolskis, A. R. *Icarus* **43,** 222 (1980).
16. Nicholson, P. D. & Jones, T. J. *IAU Circ.* No. 3515 (1980).
17. Mink, D. J., Klemola, A. R. & Elliot, J. L. *Astr. J.* **86,** 135 (1981).
18. Frogel, Jay A. & Elias, J. H. *CITO Facilities Manual* Revised edn (1980).
19. Elliot, J. L., Veverka, J. & Goguen, J. *Icarus* **26,** 387–407 (1975).
20. Baron, R. L. *et al.* (in preparation).
21. Taylor, G. E. *Mon. Not. R. astr. Soc.* **147,** 27 (1970).
22. Smoluchowski, R. *Nature* **280,** 377 (1979).
23. Gill, J. R. & Gault, B. L. *Astr. J.* **73,** S95(A) (1968).
24. Harris, A. W. *Bull. Am. astr. Soc.* **12,** 705 (1980).
25. Elliot, J. L. *et al. Astr. J.* **86,** 127 (1981).
26. Nicholson, P. D., Matthews, K. & Goldreich, P. *Astr. J.* (in the press).
27. Tyler, G. L., Marouf, E. A. & Wood, G. E. *J. geophys. Res.* (in the press).
28. Dunham, E., Elliot, J. L., Mink, D. J. & Klemola, A. R. *Astr. J.* (submitted).
29. Null, G. W., Lau, E. L., Biller, E. D. & Anderson, J. D. *Astr. J.* **86,** 456 (1981).
30. Reitsema, H. J., Hubbard, W. B. Lebofsky, L. A. & Tholen, D. J. *Science* (in the press).
31. McCord, T. B. *Astr. J.* **71,** 585 (1966).

Global satellite measurements of water vapour, wind speed and wave height

Dudley B. Chelton, Kevin J. Hussey & Michael E. Parke

Jet Propulsion Laboratory, California Institute of Technology, Pasadena, California 91109, USA

Data from the 100 days of Seasat observations in 1978 provided the first global maps of mean wind speed and wave height measured from satellites. They reveal previously unknown features in both fields and demonstrate the potential for satellite monitoring and forecasting of the worldwide sea state.

ON 28 June 1978 the United States launched Seasat, an experimental satellite to demonstrate the utility of microwave remote sensing of the ocean surface. On board were three active microwave radars (an altimeter, a scatterometer and a synthetic aperature radar) and two passive radiometers (a scanning multichannel microwave radiometer and a visible and IR radiometer). Because of their relative insensitivity to cloud cover comparedqith visual and IR sensors, microwave sensors have the advantage of all weather operations. A more detailed description of the Seasat mission is given in ref. 1. Although a short circuit in its electrical system ended the observations prematurely on 10 October 1978, Seasat provided the first global pictures from space of wave height and wind speed. Seasat also measured atmospheric liquid water, water vapour, sea-surface txperature and sea-surface topography with better accuracy than from previous satellites.

Measurements

Results of global measurements of atmospheric water vapour by the Seasat Scanning Multichannel Microwave Radiometer (SMMR) and wave height and wind speed by the Seasat altimeter (ALT) are presented here. The primary objective of ALT

0028-0836/81/500529—04$01.00

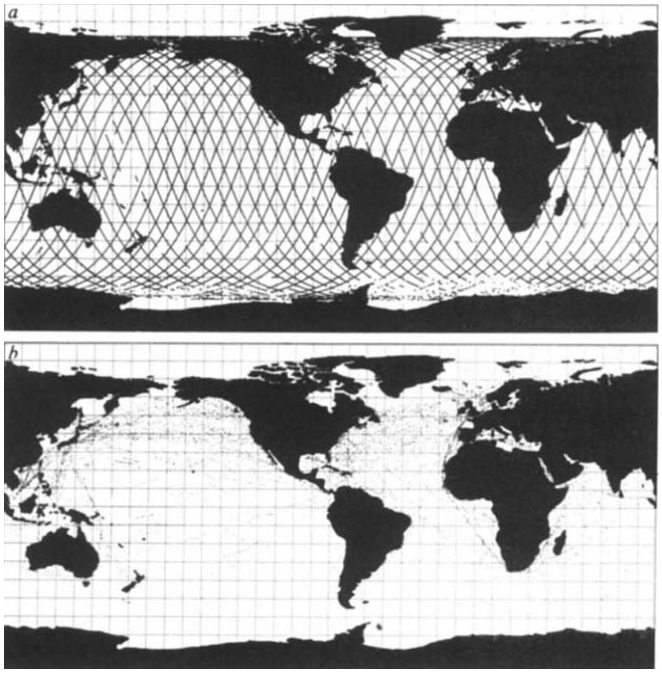

Fig. 1 Representative 3-day global data coverage by: *a*, the Seasat altimeter; and *b*, conventional ship weather reports (courtesy of D. McLain, National Marine Fisheries Service, Monterey, California). Both the examples shown are for 9–11 August 1978.

was to measure the height of the sea surface relative to a reference ellipsoid. However, the shape and power of the returned radar pulse are also used to infer wave height and wind speed at the sea surface. The 13.5-GHz Seasat altimeter is a successor of the GEOS 3 altimeter with a shorter pulse width (3.125 ns) and higher repetition rate (1,020 Hz) which lead to more precise measurements of sea surface height (better than 10 cm). The 1.59° half power beam width directed at the spacecraft nadir gives a cross track sea-surface footprint that increases from 2.4 km for 0 m wave height to 11.6 km for 20 m wave height. For the 1-s averages presented here, the along track sea-surface footprint ranges from 9.4 to 18.7 km. For typical wave heights of 3 m the ALT footprint is $\sim 5 \times 12$ km.

ALT operated intermittently, producing data over a total of 78 days. Because Seasat circled the Earth about 14 times each day at an altitude of ~800 km and an inclination of 108°, successive equatorial crossings moved in a westward direction with a separation of ~2,500 km. In 3 days, the equatorial spacing of the ground tracks was about 900 km. The full Seasat mission resulted in global coverage with ~135 km equatorial spacing of ground tracks. Typical 3-day ALT data are shown in Fig. 1*a*. The gaps in the data are due either to ALT being temporarily turned off or to a flagged error condition (such as anomalously high wave height or wind speed estimates or a satellite tilt angle beyond 0.5°). For comparison, global data from conventional ship weather reports are shown in Fig. 1*b* for the same 3-day period: ALT provides more than an order of magnitude increase in the quantity of data (131,700 compared with 7,600 observations). Even more importantly, the spatial coverage by ALT is more nearly uniform over the globe than the ship reports which tend to be concentrated along standard shipping routes in the Northern Hemisphere.

A detailed description of how the wave height can be extracted from the ALT radar return pulse is given in refs 2, 3. The waves stretch the leading edge of the returned radar pulse because of early returns from wave crests and later returns from wave troughs. Thus, the slope of the leading edge of the returned radar pulse is inversely related to the wave height. The shape of the returned pulse has been empirically related to the significant wave height (SWH) defined to be four times the r.m.s. of the crest-to-trough wave height, roughly equivalent to the average height of the one-third largest waves present in the ALT footprint. Computations of wave heights were carried out on board the satellite providing real-time wave measurements. Two simple bias corrections were later applied on the ground: a pre-launch calibration bias removal and a bias correction due to satellite tilt angle (flagged if >0.5°). A scatter plot comparing 51 buoy measurements with the ground-processed ALT estimates of SWH is shown in Fig. 2*a* (see ref. 3). The mean and r.m.s. differences (ALT minus buoy) over this sample data set are small (28 and 38 cm respectively). Apparently, the on-board processor estimates of SWH > 2 m may be biased ~50 cm high but the present sample size is too small to confirm this.

The altimeter antenna measures specular return from the nadir sea surface which is primarily determined by that part of the ocean wave spectrum with wavelengths longer than the ~2-cm wavelength of the incident radiation. As the wind speed increases, the sea-surface roughness increases and a greater fraction of the incident radiation is scattered away from the satellite. Thus the power of the returned radar pulse is inversely related to the wind speed. A more detailed description of the relationship between radar backscatter and the wind speed is given in ref. 4. A scatter plot comparing 87 buoy measurements with ALT estimates of wind speed is shown in Fig. 2*b* (see ref. 3). A direct comparison of Seasat and GEOS 3 altimeter measurements during the overlap of the two satellite missions indicated that the Seasat backscatter values were biased 1.6 dB higher than GEOS 3 (see ref. 3). The present wind estimates were generated from the Seasat ALT backscatter values by first removing this 1.6-dB bias and then using a wind speed algorithm previously derived for the GEOS 3 altimeter (see ref. 3). The mean and r.m.s. differences (ALT minus buoy) from this limited sample size are 0.25 m s^{-1} and 1.58 m s^{-1} respectively. The lack of data means that the reliability of the relationship at wind speeds in excess of 10 m s^{-1} is questionable. However, experience with GEOS 3 indicates that an altimeter can provide reliable wind speed estimates to at least 20 m s^{-1}. Investigations are underway to determine the accuracy of the Seasat ALT wind speed estimates over a broader range of conditions and from a larger data base.

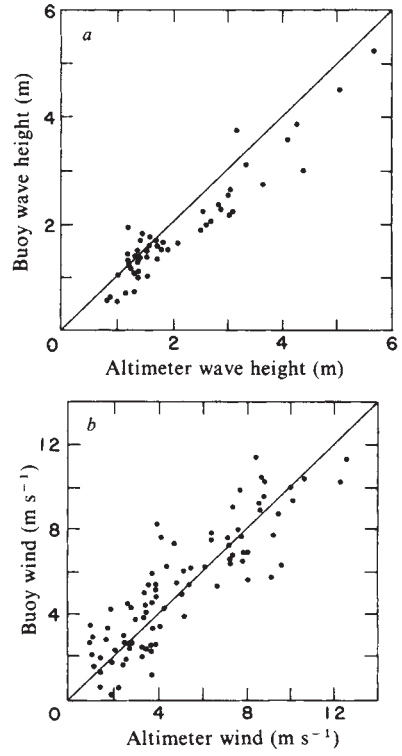

Fig. 2 *a*, Comparison of significant wave height estimated by the Seasat altimeter against 51 buoy measurements. *b*, Comparison of wind speed estimated by the Seasat altimeter against 87 buoy measurements. Data from ref. 3.

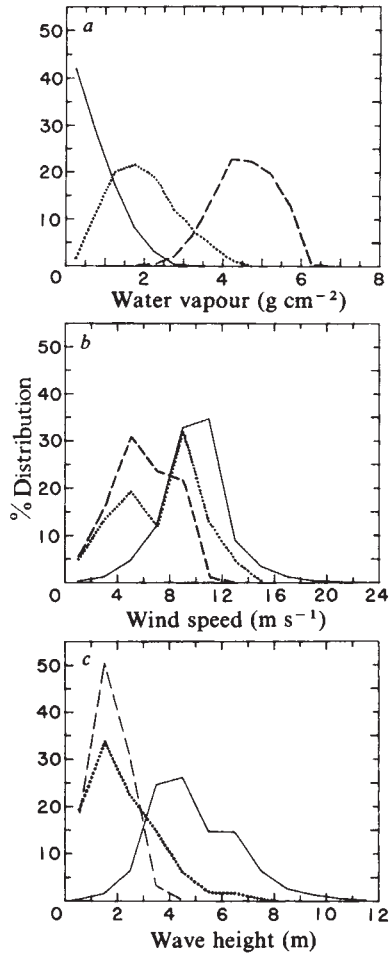

Fig. 3 Distributions of *a*, water vapour; *b*, wind speed; and *c*, wave height estimates from Seasat for the 5° lat. bands centred at 52.5° N (dotted curves), 2.5° N (dashed curves) and 52.5° S (solid curves). All observations between 7 July 1978 and 10 October 1978 are included.

An additional measurement required in any precision altimetric mission is the integrated atmospheric water vapour between the sea surface and the satellite. Water vapour estimates are necessary to make pathlength and attenuation corrections to the ALT radar pulse. On Seasat, integrated water vapour was estimated using the near nadir cell of the SMMR. The presence of water vapour between the satellite and the sea surface increases the atmospheric index of refraction which increases the effective radio frequency path length by 10–50 cm. The altimeter pathlength correction was estimated directly by a linear function of the SMMR brightness temperatures at 18, 21 and 37 GHz (both horizontal and vertical polarization). These pathlength correction estimates were then converted to total integrated atmospheric water vapour based on comparison with direct water vapour measurements from radiosondes. A detailed discussion of this procedure is given in ref. 5.

Cover picture

The 3.5-month Seasat climatological averages of integrated atmospheric water vapour, wind speed and wave height are shown on the cover. More than 3.5 million observations have been averaged globally into 2.5° square areas. The typical number of observations per 2.5° square is around 500 (higher at high latitudes where the satellite ground tracks converge). During the last month of the mission, Seasat was held in a locked orbit with 900-km equatorial spacing of ground tracks over an ~3-day repetition period. This resulted in an uneven sampling distribution over the 2.5° global grid in the 3.5-month averages presented here; 2.5° squares along the locked orbit ground track typically contained nearly twice as many sample data points over the 3.5-month period as the 2.5° squares between locked orbit ground tracks. (The regions between locked orbit ground tracks were not sampled at all from 9 September to 10 October.) Consequently, to obtain useful pictures of water vapour, wind speed and wave height, the data had to be smoothed zonally with a 7.5° running mean filter (no smoothing meridionally), so the images on the cover effectively represent 3.5-month climatological averages over 2.5° lat. by 7.5° long. areas.

The average water vapour is shown in the upper panel. The highest values are in the tropics (especially the Asian monsoon region and the intertropical convergence zone in the eastern tropical Pacific) and the lowest are at high latitudes. The effects of cool dry air blowing equatorwards over the eastern ocean basins and turning westwards as the trade winds are also evident as well as the region of high water vapour in the southern intertropical convergence zone at about lat. 10° S in the western tropical Pacific. The anomalous observations close to Antarctica are believed to be due to the presence of ice producing increased microwave brightness temperatures.

The average wind speed measured by ALT is shown in the middle panel. Several classical features of the wind field are clear: the north-east and south-east trade winds separated by the doldrums (region of light winds) in both the Atlantic and Pacific Oceans; the horse latitudes (another region of light winds) separating the trade winds from the stormy westerlies in both hemispheres; the south-east trade winds in the south equatorial Indian Ocean and the high wind speeds from the summer monsoon in the northwestern Indian Ocean. The highest wind speeds are in the Southern Hemisphere winter storm region between 50°S and Antarctica (especially south-west of Australia). The narrow region of high wind speeds in the eastern tropical Pacific at about lat. 2° N between long. 90° W and 140° W is a feature previously not seen in ship wind reports which are very sparse in this region. Note also the jet of high wind speed off the coast of California (see ref. 6).

The lower panel shows the average significant wave height during the Seasat mission. This is the first accurate picture of global wave conditions and, we believe, the first reliable measurement by any method of ocean waves for winter season in the Southern Hemisphere. It reveals some interesting features. The average wave height is small in the summer Northern Hemisphere (generally 2–3 m) and the largest waves are located in the winter Southern Ocean where the wind speeds are highest (especially south-west of Australia where mean wave height is >5.5 m). The smallest waves are found in the western Atlantic and Pacific Oceans (average height <1.5 m) in regions of light winds. We expect that further analysis of the ALT wave height data will ultimately lead to a better understanding of the process of wind wave generation.

Discussion

The fact that the 2.1-m contour between 50° and 55° N in the North Pacific does not extend all the way to the coast can probably be explained by the coarse 2.5° lat. by 2.5° long. resolution of the data presented here. Examination of finer-resolution data in this region reveals that the apparent decrease in wave height in the 2.5° averages close to the coast is due to the presence of a distinct wave shadow behind Queen Charlotte Island (the largest of the many islands off the west coast of Canada). In the finer-resolution data, the 2.1-m waves extend all the way to the western shores of these islands but wave heights are <1 m behind the islands.

Note that ice in the ALT footprint causes very erratic behaviour in the shape and power of the returned radar pulse which typically results in rapid changes from very high to very low wave height estimates by ALT. This anomalous behaviour is flagged on the ALT geophysical data records gferated fromhhe sensor data by the Jet Propulsion Laboratory, thus providing a potential method for mapping ice coverage from altimeter measurements. Anomalously high wave height estimates have been excluded from our data so that wave height estimates over ice are small. Thus the ice-covered area is represented in the

wave height map on the cover by the light-coloured region close to Antarctica.

While climatological averages emphasize geographical differences within each field, they give no indication of the range of conditions likely to be encountered in a particular region at different times. The rather striking zonal banding of each of the fields suggests that latitudinal distributions can provide some initial insight into water vapour, wind speed and wave height variability during the Seasat mission. The probability distributions of each of the three fields for the three 5° lat. bands centred at 52.5° N, 2.5° N and 52.5° S are shown in Fig. 3.

The features evident in the water vapour distributions in Fig. 3*a* are not surprising. They clearly show the higher integrated water vapour levels found in the tropics. Only 2% of the observations in the equatorial band were <3 g cm^{-2} while 96% of the observations in the high southern latitude band were <2 g cm^{-2}. This reflects the lower water vapour saturation level of the cold Southern Hemisphere winter air. The cool high northern latitude band shows intermediate water vapour values with 75% of the observations between 1 and 3 g cm^{-2}. A more detailed study of the water vapour estimates might be useful in climatological studies of the global time variability of the latent heat of vapourization transferred from the ocean to the atmosphere.

The wind speed distributions in Fig. 3*b* show some unexpected features. As the high southern latitude band is in the winter storm region, the higher wind speeds in this band are not surprising. Large variations might also be expected due to the passage of individual storms. However, the winds in this band seem to be relatively steady: 68% of the observations were between 8 and 12 m s^{-1}. In comparison, the trade winds of the equatorial band, which are noted for their steadiness, show a peak at much lower wind speeds but a broader distribution: 76% of the observations were between 4 and 10 m s^{-1}. Another curious feature is the probability distribution for the high northern latitude band: the range of wind speeds is broader than either of the other two bands but there are two pronounced peaks, a primary peak at 9 m s^{-1} and a secondary peak at 5 m s^{-1}. Present studies are aimed at determining whether the double peaks arise from zonal averaging of an inhomogeneous field or whether they reflect a seasonal change in the wind speed distribution during the 3.5-month period.

The wave height distributions are shown in Fig. 3*c*. The equatorial band has the narrowest range of wave conditions: 70% of the waves were <2 m and virtually none were >4 m. In comparison, only 50% of the waves in the high northern latitude band were <2 m and 5% were >5 m. In contrast to both the equatorial and high northern latitude bands, the peak in the wave height distribution in the stormy high southern latitude band is at a much higher value (3.5 m as opposed to 1.5 m) and the range of wave conditions is much wider. Only 2% of the waves observed were <2 m and over 40% were >5 m. The secondary peak at 6.5 m is rather puzzling; it is difficult to explain in terms of wind forcing as there is no similar double-peaked structure in the wind speed distribution in this latitudinal band. The double peaks probably result from zonal averaging of the large wave heights south and west of Australia with the smaller wave heights elsewhere in this 5° latitudinal band (see cover).

There is no way of knowing at present whether the 3.5-month average wind speed and wave heights presented here are typical for this time of year. However, these geophysical maps demonstrate the unique ability of satellites to provide global measurements of wind and wave conditions. This will be especially useful in data-sparse regions such as the Southern Hemisphere (see Fig. 1*b*) where present forecasts of weather and sea states are extremely unreliable. Even in the Northern Hemisphere, forecasting skill is limited in many regions by sparse data coverage over the oceans. An operational altimetric mission could improve worldwide sea state forecasting.

This research was carried out at the Jet Propulsion Laboratory, California Institute of Technology, under contract with NASA. L. Fedor and G. Brown made their results (Fig. 2) available before publication of their own work.

Received 15 July; accepted 12 October 1981.

1. *Science* **204**, 1405–1424 (1979).
2. Walsh, J., Uliana, E. A. & Yaplee, B. S. *Bound. Layer Met.* **13**, 263–276 (1978).
3. Fedor, L. S. & Brown, G. S. *J. geophys. Res.* (in the press).
4. Brown, G. S. *J. geophys. Res.* **84(B8)**, 3974–3978 (1979).
5. Tapley, B. D., Lundberg, J. B. & Born, G. H. *J. geophys. Res.* (in the press).
6. Nelson, C. S. *NOAA Tech. Rep. NMFS SSRF-714* (1977).

Dipoles of the α-helix and β-sheet: their role in protein folding

Wim G. J. Hol*, Louis M. Halie* & Christian Sander†

* Laboratory of Chemical Physics, Department of Chemistry, University of Groningen, Nijenborgh 16, 9747 AG Groningen, The Netherlands
† Biophysics Department, Max Planck Institute of Medical Research, Jahnstrasse 29, Heidelberg, FRG

As a result of the regular arrangement of peptide dipoles in secondary structure segments and the low effective dielectric constant in hydrophobic cores, the electrostatic energy of a protein is very sensitive to the relative orientation of the segments. We provide here evidence that the alignment of secondary structure dipoles is significant in determining the three-dimensional structure of globular proteins.

IT has long been known that in the α-helix the alignment of the peptide dipoles parallel to the helix axis gives rise to a macrodipole of considerable strength (for review see ref. 1). With a dipole moment for each peptide unit of ~3.5 D, a helix of, for example, 10 residues has a dipole moment of 34 D, as 97% of the peptide dipole points in the direction of the helix axis. It has been shown[2] for points near the helix termini that the effect of the helix dipole is equivalent to the effect of half a positive unit charge at the N-terminus of the helix and half a negative charge at the C-terminus. The same authors provided evidence that the considerable electric field due to the helix dipole moment is used by proteins in: (1) binding negatively-charged groups, such as phosphate groups; (2) rendering protein side chains located near the N-terminus more nucleophilic; and, (3) stabilizing charged transition states or intermediates along the catalytic pathway. So far ~20 helices have been observed which bind negatively-charged groups near their N-termini. Another 10 proteins have their active site close to the N-terminus of a helix (W.G.J.H., unpublished results). For papain, an extensive quantum mechanical calculation[3] showed that the field generated by the helix dipole is a major factor in the stabilization of the sulphhydryl–imidazole ion pair essential in

0028-0836/81/500532—05$01.00